

Doppler Cardiogram: A Remote Detection of Human Heart Activities

Shuqin Dong, Yi Zhang, Chao Ma[✉], Chengkai Zhu, Zhitao Gu, Qinyi Lv[✉], Bin Zhang, Changzhi Li[✉], *Senior Member, IEEE*, and Lixin Ran[✉]

Abstract—Most medical instruments invented to measure human heart activities, such as electrocardiograms (ECGs), rely on contact electrodes. This causes discomfort and limits application scenarios. Remote acquisition of μ V-level bioelectrical cardiac signals through ECG measurement is theoretically challenging. Based on the analysis of magnetic resonance imaging to the volume change of human hearts, we found that a single radar sensor can be used to remotely detect a Doppler cardiogram (DCG) at a distance up to 1 m, by retrieving Doppler signals induced by combined atrial and ventricular motions conducted to the skin of the back chest. This DCG can provide all the timing information of the P-wave, QRS-waves, and T-wave carried in ECGs. The implemented miniature remote sensor could be an ideal portable instrument for patients, such as burn victims, extending application scenarios to personal healthcare, battlefield rescue, and others.

Index Terms—Cardiac motion, Doppler radar sensor (DRS), human cardiogram, random sample consensus (RSC), remote sensing.

I. INTRODUCTION

IN THE modern world, cardiovascular diseases have become the leading cause of death [1]. In the diagnosis and prevention of cardiovascular diseases, measurement and long-term monitoring of human cardiograms are indispensable [2]. Based on different principles and technologies, medical instruments have been invented to measure different cardiograms [3]–[9]. To date, commercial cardiogram instruments have been capable of measuring electrocardiogram (ECG) [3], ultrasonic cardiogram (UCG) [4], phonocardiogram (PCG) [5], impedance cardiogram (ICG) [6], ballistocardiogram (BCG) [7], and live cardiograms based on magnetic resonance imaging (MRI) [8], [9]. So far, to the best of our knowledge, except for the radiative MRI cardiogram, which is expensive and unsuitable for daily healthcare, all the other cardiograms have to be measured with contact sensors, such as ECG electrodes and UCG probes. Especially, the measurements of the most widely used ECGs rely on multiple contact electrodes to detect

μ V-level bioelectrical cardiac signals. Remote measurements of ECGs have been considered theoretically challenging, if not impossible.

Contact cardiogram measurements will cause discomfort and limit their application scenarios. For instance, contact ECG measurements can be applied for neither patients such as burn victims nor scenarios of personal healthcare and battlefield rescue. Implementing noncontact measurements of human cardiograms are therefore highly desirable.

With the rapid development of radio frequency and microwave integrated circuits in the past decade, miniaturized continuous-wave Doppler radar sensors (DRSs) have been developed for noncontact detection of different moving objects in short-range indoor environments [10], [11]. With different architectures such as zero intermediate frequency (zero-IF) [12], digital-IF [13], self-injection-lock [14], six-port [15], and single-in multiple-out (SIMO) [16], [17] architectures, such DRSs can be used to detect various motions, such as human and animal biosignals [18], [19], structural vibration of buildings and bridges [20], [21], human gestures and gaits [22], and mechanical motions such as linear stepped motion of a translation stage and rotation of wind turbine blades [23], [24]. The scale of the detectable motions ranges from submillimeters to meters [13].

For different DRS architectures, algorithms used to retrieve Doppler signals from the electric fields scattered by different moving objects have also been proposed. Typical examples include the small-angle approximation [26] for zero-IF architectures and extended differential and cross-multiply (DACM) [27] and arcsine algorithm [28] for balanced receivers, such as the digital-IF receiver. The abovementioned advances showed promising applications of DRSs in various areas.

In this article, based on the analysis of MRI to the volume change of human hearts, we found that a single DRS can be used to remotely measure a Doppler cardiogram (DCG) by retrieving the Doppler signal induced by the combined atrial and ventricular motions conducted to the skin on the back chest. This DCG can provide the timing information of the P-wave, QRS-waves, and T-wave in ECGs. The implemented miniature remote sensor could be an ideal portable instrument, extending application scenarios to personal healthcare, battlefield rescue, and many others.

This article is organized as follows. Section II introduces the diastole and systole periods of the atriums and ventricles,

Manuscript received July 10, 2019; revised August 18, 2019 and September 23, 2019; accepted October 10, 2019. Date of publication November 19, 2019; date of current version March 4, 2020. This work was supported by the NSFC under Grant 61771421. (Corresponding author: Lixin Ran.)

S. Dong, Y. Zhang, C. Ma, C. Zhu, Z. Gu, Q. Lv, B. Zhang, and L. Ran are with the Laboratory of Applied Research on Electromagnetics (ARE), Zhejiang University, Hangzhou 310027, China (e-mail: ranlx@zju.edu.cn).

C. Li is with the Department of Electrical and Computer Engineering, Texas Tech University, Lubbock, TX 79409 USA (e-mail: changzhi.li@ttu.edu).

Color versions of one or more of the figures in this article are available online at <http://ieeexplore.ieee.org>.

Digital Object Identifier 10.1109/TMTT.2019.2948844

0018-9480 © 2019 IEEE. Personal use is permitted, but republication/redistribution requires IEEE permission.

See <https://www.ieee.org/publications/rights/index.html> for more information.

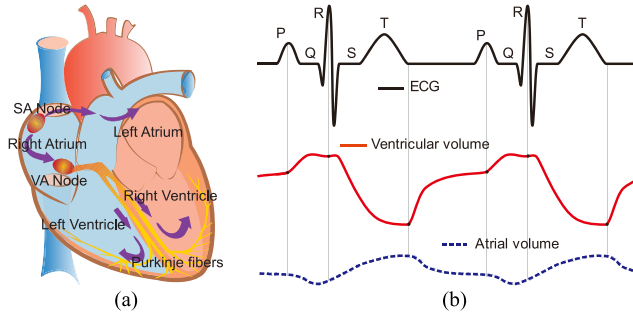


Fig. 1. Bioelectrical and mechanical activities of human hearts. (a) Conduction of the bioelectrical excitations. (b) Human ECG and the diastole and systole periods of atriums and ventricles.

and the correspondence between the atrial and ventricular volume change and the cardiac bioelectrical signals, which provides the theoretical basis of this article. It then lays out the theoretical foundation for the DCG detection. Section III demonstrates the experimental detection of the DCGs. Finally, a conclusion is drawn in Section IV.

II. METHODS

A. Problem Description

The human heart is a cone-shaped muscular organ located in between the left and right lungs in the middle compartment of a chest. Its function is to pump blood through the atriums and ventricles into the pulmonary or blood circulatory systems, providing oxygen and recycling carbon dioxide to and from the human body [30]. This cardiac motion is rhythmic, synchronous with the bioelectrical “excitations” spontaneously generated in the sinoatrial (SA) node and conducted from the atriums to ventricles [29]. The conducting paths are shown in Fig. 1(a). Such bioelectrical activity can be detected by electrodes placed at different locations on the skin, and the plotted “action potentials” is known as the ECG [3].

The diagram in Fig. 1(b) illustrates two complete periods of such an ECG as well as the volume changes of the atriums and ventricles at the same time. In each period, the ECG includes a “P wave,” a “QRS-waves,” and a “T wave” [3]. The P wave reflects the initiation of a bioelectrical impulse at the SA node and the activation of the atria, during which the atrium contracts and ejects blood into the ventricles. The flat P-R segment represents the short interval during which the bioelectrical signal is delayed at the atrioventricular (AV) node, which allows blood to be fully ejected into the ventricles. The QRS-waves represents the quick impulse that propagates from the AV node down through the Purkinje fibers, causing the ventricles to contract. The left ventricle continuously contracts and ejects blood into the aorta until the end of the T wave.

Obviously, the contraction and relaxation of atriums and ventricles will cause the change of their volumes with the same rhythm as that of the ECG. In Fig. 1(b), the diastole and systole periods of atriums and ventricles are also illustrated. It is reasonable to consider that the characteristic points (CPs), at the beginnings and ends of the ventricular contractions and relaxations, are synchronous with the corresponding CPs

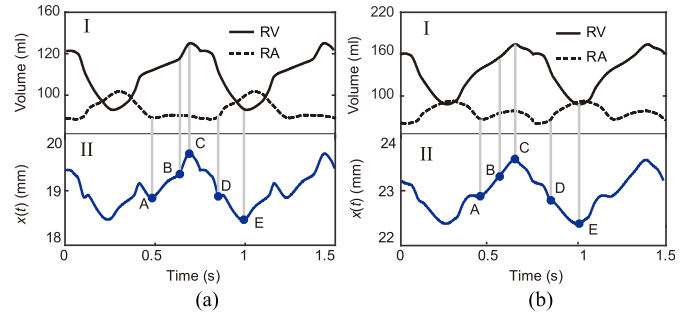


Fig. 2. Volume changes of the right atrium (RA) and ventricle (RV) with respect to time. (a) Healthy person. (b) Patient with a tetralogy of Fallot disease. Figures were replicated based on MRI images reported in [9].

on ECGs. It implies that if the cardiac volume change can be measured, a new type of human cardiogram may be obtained.

Previously, a preliminary noncontact detection of the cardiac motion has been conducted based on commercial instruments [12]. Due to the unsatisfactory signal-to-noise ratio (SNR), the retrieved CPs did not look convincing. In the following, such cardiac volume changes will be detected using a highly integrated, linear, and sensitive DRS.

B. Cardiac Volume Change Conducted to the Skin

A DRS transmits a continuous wave to illuminate a moving object. It retrieves the Doppler signal from the backscattered field. In this article, this “moving object” is the skin surface surrounding the human chest. Since human blood and most of tissues are highly conductive [30], the illuminating wave can hardly penetrate into the human chest and reach the heart, especially at millimeter-wave frequencies. The motion actually detected by a DRS is the cardiac volume change conducted to the skin. Note that such a motion is a “combined motion” due to the simultaneous contraction and relaxation of both the atriums and the ventricles.

To investigate if the ECG CPs still exist in such a combined motion, we tried to synthesize this motion based on the experimental data of atrial and ventricular volume changes measured by a cardiac MRI [9].

The panels denoted as I in Fig. 2(a) and (b) show the experimental time-variant volume changes of the atrium [$V_a(t)$] and the ventricle [$V_v(t)$] of a healthy person and a person with tetralogy of Fallot disease, respectively. Such curves were replicated from [9, Fig. 2]. For simplicity, we assume that both the atriums and the ventricles are cylinder-like, and the total radial component, denoted as $x(t)$, of the combined cylindrical volume changes conducted to the skin surface can be estimated as

$$x(t) \propto \sqrt{V_a(t)} + \sqrt{V_v(t)}. \quad (1)$$

Such combined motions are plotted in the panels denoted as II in Fig. 2(a) and (b). It is interesting to observe that the combined volume change even includes more CPs, as represented by the blue dots marked from A to E. More importantly, the skin motions calculated for the healthy person and the

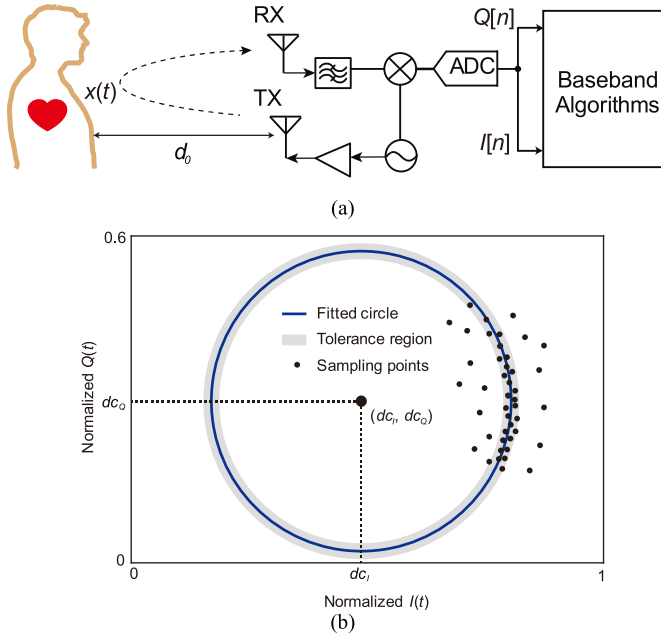


Fig. 3. Architecture of the DRS and the compensation of the dc offsets. (a) Block diagram. (b) Illustration of the statistical dc offset compensation.

patient with cardiac disease are notably different. This implies that such a DCG may be potentially used in the diagnosis of cardiac diseases related to abnormal atrial and ventricular abstractions and relaxations, which cannot be identified from the ECG.

C. Doppler Detection of the Cardiac Motion

Fig. 3(a) shows the block diagram of a single-in single-out (SISO) DRS used in this article to detect the combined motion $x(t)$. It consists of a transmitting antenna, a receiving antenna, a zero-IF front end, and a quadrature baseband running algorithms for retrieving Doppler signals. According to [38], the detected in-phase (I) and quadrature-phase (Q) signals scattered by the skin can be described as

$$\begin{cases} I(t) = A_I(t) \cos \left[\theta_d + \frac{4\pi x(t)}{\lambda} + \varphi_n(t) \right] + dc_I(t) \\ Q(t) = A_Q(t) \sin \left[\theta_d + \frac{4\pi x(t)}{\lambda} + \varphi_n(t) \right] + dc_Q(t) \end{cases} \quad (2)$$

where λ is the wavelength, $\varphi_n(t)$ is the total residual phase noise, θ_d is the phase delay due to the distance between the moving object and antennas, $A_I(t)/A_Q(t)$ are the amplitudes of the quadrature signals, and $dc_I(t)/dc_Q(t)$ are the dc offsets due to the stationary background scattering and the zero-RF receiver.

In previous studies, how to linearly retrieve the motion $x(t)$ from (2) has been discussed extensively [13], [31], [37]–[41]. One effective approach is to use the arctangent function based on the balanced sine and cosine items. In this case

$$x(t) = \frac{\lambda}{4\pi} \left\{ \arctan \frac{[Q(t) - dc_Q(t)]/A_Q(t)}{[I(t) - dc_I(t)]/A_I(t)} - \theta_d - \varphi_n(t) \right\}. \quad (3)$$

In (2), θ_d is a constant. For a high-performance DRS, $\varphi_n(t)$ can be ignored. The imbalance between $A_I(t)$ and $A_Q(t)$ can be calibrated in the digital domain. Therefore, if the dc offsets $dc_I(t)$ and $dc_Q(t)$ can be compensated, the motion $x(t)$ can be linearly retrieved by applying an extended DACM algorithm in the digital domain, that is

$$x[n] = \sum_{k=2}^n \frac{I[k]\{Q[k] - Q[k-1]\} - \{I[k] - I[k-1]\}Q[k]}{I[k]^2 + Q[k]^2}. \quad (4)$$

To compensate for $dc_I(t)$ and $dc_Q(t)$, for balanced $A_I(t)$ and $A_Q(t)$ and neglectable θ_d and $\varphi_n(t)$, (2) can be rewritten as

$$[I(t) - dc_I(t)]^2 + [Q(t) - dc_Q(t)]^2 = A^2(t) \quad (5)$$

where $A_I = A_Q = A$. It is seen that ideally, the detected $I(t)$ and $Q(t)$ would locate on a circle with the balanced amplitude as the radius and $[dc_I(t), dc_Q(t)]$ as the center. Therefore, the essence of the dc offset compensation is to determine the center of the circle defined by (5).

For small-scale, subwavelength motions such as the cardiac motion conducted to the skin, the constellation diagram consisting of the sampling points of I/Q signals will be located on a segment of arc, instead of an entire circle. In the presence of noise and/or interfering motions, such points will be scattered along the arc, as shown in Fig. 3(b).

Previously, the gradient descent (GD) algorithm proposed in [13] had been used to determine the circle center. However, it does not work when the scattered points caused by interfering motions are distant from the arc. In the scenario of noncontact, continuous detection of human cardiac motion, such interfering motions, can be a motion combined with the cardiac motion under detection, such as a random body movement, or an independent motion, such as a hand action [17], [31].

To solve this problem, we used, in this article, a statistical random sample consensus (RSC) algorithm previously used in computer visions [32]. As a robust pattern fitting approach, it works in the presence of distant scattered points by finding a pattern that matches the most of the points. In our scenario, this pattern is a circular arc with its center and radius to be determined.

To apply the RSC algorithm, three sampling points can be randomly chosen in all the sampling points, based on which an initial circle containing the arc can be constructed [32]. Then, an annulus region, whose radial width defines the error tolerance to determine whether a sampling point is close enough to the arc, can be determined, as shown in Fig. 3(b). Finally, the ratio r between the numbers of the sampling points inside and outside the annulus region can be calculated. Such a process can be repeated until the ratio reaches the desired percentage, such as 95% used in this article. According to the RSC theory, the probability p that the desired result can be obtained after N iterations can be determined by

$$p = 1 - (1 - w^3)^N \quad (6)$$

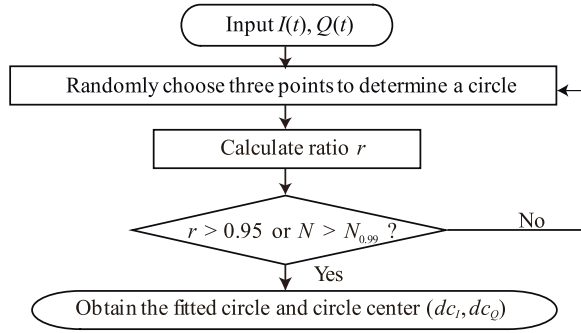


Fig. 4. Flowchart of the RSC algorithm.

where w is the probability that a point is inside the tolerance region. Then, the number of iterations N can be determined by

$$N = \log(1 - p) / \log(1 - (1 - w)^3). \quad (7)$$

In practice, p is usually set as 0.99 [34]. Here, we denote N for $p = 0.99$ as $N_{0.99}$. Depending on the noises and interfering motions, w varies in a large range. For w changing from 0.1 to 0.9, $N_{0.99}$ ranges between 2 and 1000. Fig. 4 shows the flowchart of the RSC algorithm, in which $N_{0.99}$ can be considered as the maximum iteration number used to terminate the iteration if the expected ratio r cannot be reached.

To verify the effectiveness of the RSC algorithm and compare its performance with the GD approach, we numerically simulated the dc offset compensation for I/Q signals scattered by a 20-s sinusoidal cardiac motion $x_1(t)$ in the presence of noises and a 5-s interfering motion $x_2(t)$.

In the simulation, we assume $x_1(t) = 0.02\lambda \sin(2\pi t)$, $x_2(t) = 0.1\lambda t$, and the 5-s interference occurred in the middle of the 20-s $x_1(t)$. In the first case, $x_2(t)$ is combined with $x_1(t)$ so that the field scattered by this combined motion would have a phase item, such as $\sin(4\pi(x_1(t) + x_2(t))/\lambda)$. In the second case, $x_1(t)$ and $x_2(t)$ are independent so that the scattered field would have a form, such as $A_1 \sin(4\pi(x_1(t)/\lambda)) + A_2 \sin(4\pi(x_2(t)/\lambda))$. In both cases, Gaussian noises were added to the scattered fields so that the SNRs of the received signals are both 20 dB.

Fig. 5(a) and (b) shows the constellation diagrams in the presence of the abovementioned noises and interfering motions and the circles reconstructed by the RSC and the GD algorithms, respectively. Fig. 5(c) and (d) shows the corresponding motions reconstructed by the extended DACM algorithm. It is seen that in the presence of large-scale, short-time interfering motions, while the circles determined by the GD algorithm are both incorrect, the RSC algorithm is able to find the circle centers with small errors.

It should be noted that neither the GD nor the RSC algorithm would work during the interference. The purpose of using the RSC algorithm is to ensure that during the entire measurement, the dc offset can remain unchanged, regardless of the presence of unwanted interfering motions. It means that all the DCG cycles can be retrieved with the same dc offset, ensuring the effectiveness of the cycles retrieved in the absence of interference. It will facilitate the interception of DCG cycles detected in the absence of interference.

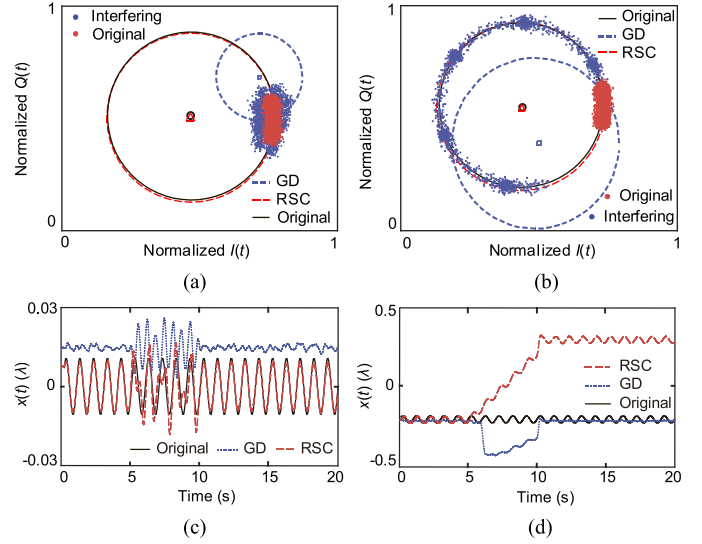


Fig. 5. Comparison between the RSC and the GD algorithms. (a) and (b) Constellation diagrams and reconstructed circles in the presence of interfering independent and combined motions, respectively. (c) and (d) Motions recovered by RSC and GD algorithms, respectively. A Butterworth low-pass filtering has been performed to the results calculated by the extended DACM algorithm.

D. Sensitivity and Linearity of the DRS

To measure the cardiac motions conducted to skin, very high sensitivity and linearity of the DRS will be required. In this article, a novel approach was proposed to measure such specifications by producing an ideal, amplitude controllable sinusoidal motion using a simple pendulum [35], [36], which can be easily established with a suspension frame, a thin wire, and a pendulum ball.

According to [35], if the angle θ of the pendulum swing is smaller than a threshold angle, normally considered as 0.1 rad, the pendulum swing can be approximated as a linear harmonic oscillation with its frequency that only depends on the length L of the suspension wire, that is

$$f = 1/2\pi \sqrt{L/g} \quad (8)$$

where g is the acceleration of local gravity. Such a harmonic motion can be analytically expressed as

$$x(t) = L\theta \cos(2\pi ft). \quad (9)$$

To determine the linearity, this sinusoidal motion can be measured by the DRS using the algorithms discussed earlier, and the specification of “harmonic suppression” previously used in evaluating the linearity of amplifiers can be used to evaluate the linearity of the DRS.

Similarly, the decay of the pendulum swing measured by the DRS can be used to determine its sensitivity by examining the smallest pendulum swing that can be convincingly detected with a threshold SNR of the I/Q signals.

III. MEASUREMENT

A. Measurement Setup

Fig. 6(a) shows the block diagram of the DRS used to measure the DCG based on a 24-GHz silicon-germanium

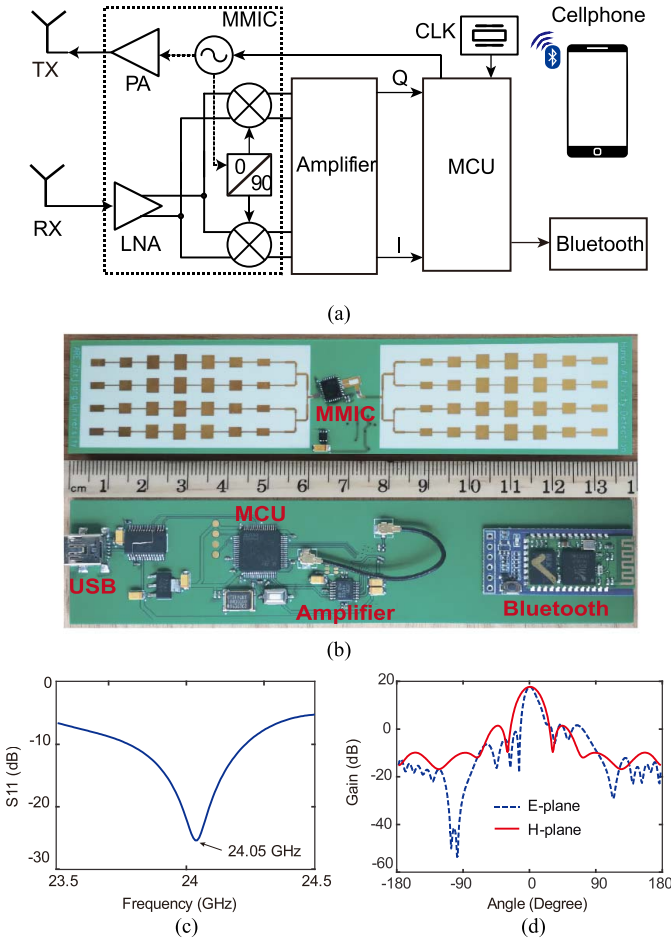


Fig. 6. Design and implementation of the 24-GHz DRS. (a) Block diagram. (b) Board-integrated DRS with a Bluetooth interface. (c) S_{11} of the series-fed patch array. (d) Radiation patterns of the series-fed patch array.

TABLE I
MAIN DEVICES USED IN THE DRS

ID	Device	Manufacturer	Function
1	BGT24MTR11	Infineon	24-GHz transceiver MMIC
2	HC-05	Motorola	Bluetooth module
3	INA2331	Texas Instruments	Instrumentation amplifier
4	STM32	ST Electronics	32-bit microcontroller

millimeter-wave integrated circuit (MMIC), Infineon BGT24MTR11. Designed with a differential architecture from the RF front end to the quadrature baseband, it has a high noise performance and is suitable for detecting small motions. The main devices used to implement the DRS are listed in Table I.

Fig. 6(b) shows the implemented board-integrated DRS. The substrate used is Rogers 4350B, whose dielectric constant and the loss tangent are 3.48 and 0.0037, respectively. The DRS can be powered by a power bank through a standard USB port. With the assistance of a Bluetooth interface, the I/Q data sampled by the built-in 12-bit analog-to-digital converters (ADCs) inside the MCU can be conveniently transmitted to a cellphone. A unique characteristic of this design is the use of

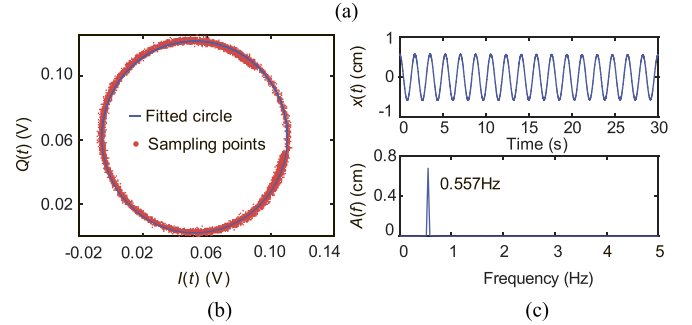
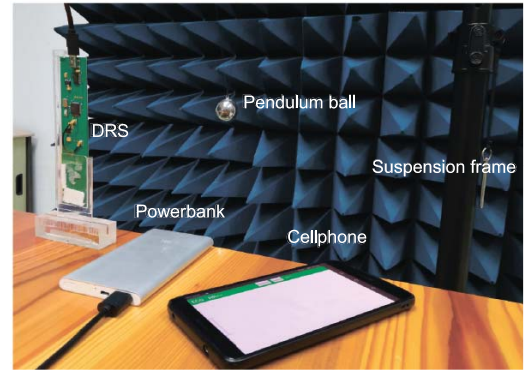


Fig. 7. Performance measurement of the linearity. (a) Experimental setup. (b) Constellation diagram and the fit circle. (c) Recovered pendulum motion and the corresponding spectrum.

a pair of high-gain patch arrays, each consisting of four groups of seven-series-fed radiation elements. It was printed on the same PCB layer with the MMIC, achieving minimized size and avoiding potential losses and impedance mismatch due to the use of millimeter-wave cables and adaptors. S_{11} of such antennas is given in Fig. 6(c). The gain reaches 17.7 dBi, with 3-dB beamwidths around 13.5° and 25.4° in the E - and H -planes, respectively, as shown in Fig. 6(d). According to the datasheet of the MMIC, the transmitting power is 15 dBm, the voltage conversation gain of the receiver is 26 dB, and the amplitude and phase imbalances of the I/Q channels are less than 1 dB and 10° , respectively.

B. Performance Measurement

Before the measurement of cardiac motions, the linearity and the sensitivity of the DRS were measured first. Fig. 7(a) shows the setup for the linearity measurement. To generate an ideal sinusoidal movement, a simple pendulum consisting of a suspension frame and a 1.5-cm-diameter steel ball suspended by an 80-cm-long thin wire was established. According to (8), the pendulum frequency of the pendulum swing can be estimated as 0.6 Hz. The pendulum ball is approximately 40 cm away from the DRS. The initial pendulum amplitude is around 0.5 cm, corresponding to a 0.014-rad angle of the pendulum swing, much smaller than the threshold of 0.1 rad. According to Section II-D, such a pendulum swing can be considered as a pure harmonic motion.

The constellation diagram of a segment of 30-s raw I/Q data sampled by the DRS is shown in Fig. 7(b), along with the circle fit by the RSC algorithm. With a 350 per second

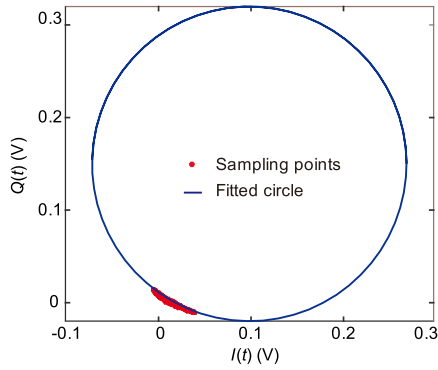


Fig. 8. I/Q signals scattered by a pendulum ball for the sensitivity test.

sampling rate, the constellation consists of 10500 sampling points. Based on the circle fit by the RSC algorithm and the extended DACM algorithm, the pendulum motion can be retrieved. Fig. 7(c) shows a segment of 30-s pendulum swing and its spectrum. The detected pendulum frequency is 0.557 Hz, in agreement with the estimated 0.6 Hz. The spectrum of retrieved motion is very clean, without any visible harmonics. This result complies with the theoretical expectation, implying a very high linearity for the measurement of motions.

It should be noted that (8) was derived under a mass-point equivalence. In comparison, the experimental pendulum is with a 1.5-cm-diameter steel ball. In the meantime, the 80-cm-long suspension wire was also approximated. The error between the 0.557- and 0.6-Hz frequencies may come from these differences. However, this amplitude error will not affect the accuracy of the DCG, because Doppler signals caused by moving objects are modulated on the phase, instead of the amplitude.

Then, the sensitivity of the DRS in measuring the smallest motions was tested by measuring the same pendulum with a 4-cm suspension wire. The purpose of using a shortened wire is to increase the pendulum frequency. In this case, the pendulum swing will decay rapidly so that the pendulum amplitude detected in a short time can vary from very large to below the noise floor. Then, the sensitivity of this DSR can be determined as the pendulum amplitude that corresponds to a threshold of the DRS baseband SNR, which is set as 10 dB in this article.

Fig. 8 shows the raw I/Q signals detected for a segment of 150-s pendulum swing and the circle fit by the RSC method. It is seen that all the sampled points are located in the vicinity of an arc. Fig. 9(a) shows the reconstructed 150-s pendulum swing and the time-varying SNR. It is seen that as the detected pendulum amplitude decays gradually from nearly 200 μm to the noise floor, the SNR decays from 40 to 0 dB. For more details, the five insets show the zoomed-in segments selected with different SNRs. Fig. 9(b) shows the spectra of the corresponding segments shown in the insets. It is seen that if we chose the 10-dB SNR as the detecting threshold, the sensitivity of this DRS to detect the minimum amplitude of a sinusoidal motion can be as small as 4 μm .

C. Measurement of the DCG

The noncontact measurement of the DCG was performed in a regular laboratory environment, as shown in Fig. 10(a). During the measurement, a female subject sat still leaning on the back of a chair. The DRS was placed around 40-cm away from her back. For comparison, a portable ECG instrument also with a Bluetooth interface, HEAL FORCE PC-80B, was simultaneously used to detect the ECG using electrodes placed on her wrists and chest. A receiving Bluetooth interface was programmed on the cellphone end, to synchronously read the digitized data from both the DRS and the ECG instrument, so that the alignment of the corresponding timing points in the detected ECG and DCG can be convincingly verified.

In the measurement, three electrodes were attached to the front chest and the two wrists of the subject. In the meantime, the radar sensor was used to detect the field scattered from the back of the subject. Therefore, the electrodes and wires in the front of the subject will not interfere with the radar sensor.

Fig. 10(b) shows the constellation of a 25-s I/Q signal detected by the DRS in a measurement. In the first 15 s of this measurement, the subject kept normal breath and used her hands to manipulate the ECG instrument. In the following 10 s, the subject held her breath. The sampling points with different colors show the segments with and without breath and interfering actions. In the presence of the interfering breath and hand actions, the RSC method is used to compensate for the dc offsets, and the fit circle is shown in red solid line. Under the same condition, the circle fit using the GD algorithm was also provided for comparison, which is shown in the blue dashed line.

Panels I and II in Fig. 11 show the last 10-s segments of the ECG detected by the PC-80B and the DCG detected by the DRS. The recovered cardiac motion, i.e., $x(t)$ described in (3), is plotted in blue. The amplitude of this motion is between 75 and 157 μm , much larger than the 4- μm sensitivity of the DRS. It can be seen that along the cardiac motion, there exists a very slow random body movement, resulting in a positive slope of the curve. If needed, this slope can be calibrated using the polynomial fitting approach proposed in [31].

To locate the CPs A to E denoted in Fig. 2, the velocity and acceleration of $x(t)$ were calculated, as shown in panels III and IV. It is seen that the A, C, D, and E points in a cycle can be located by the corresponding zeros or extreme points on the $v(t)$ or $v'(t)$ curves, and the B point can be located by the dent on the $v(t)$ curve to the right of point A. It can be seen that although, in some DCG cycles, the rising slope containing the B point looks quite smooth, the change on this slope can be notably “amplified” by taking a derivative to $x(t)$. It is seen that all the dents align to the peaks of the P waves, and most of the alignments are accurate. A few larger alignment errors appear in the 11th, 12th, and 13th cycles, which may be related to the very slow random body movement. In practice, a program can be developed to automatically locate such CPs, which has clear correspondence with respect to those marked in panel II of Fig. 2(a). The overall shape of the detected DCG is also very similar to the combined volume change synthesized by the experimental

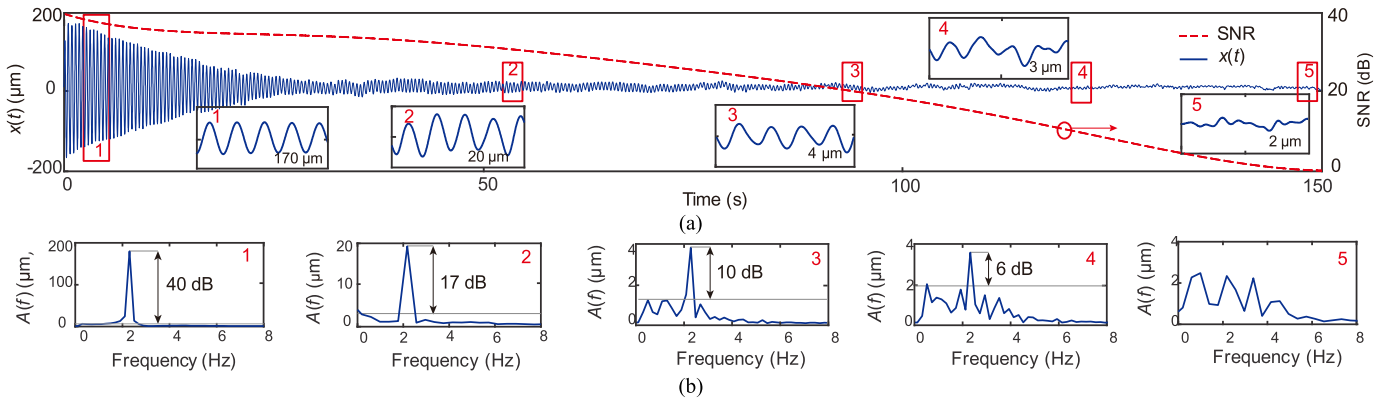


Fig. 9. (a) Demodulated pendulum swing and the SNR. (b) Spectra of five selected segments.

TABLE II
CORRESPONDENCE BETWEEN CPs AND THE DCG AND ECG

CP	DCG	ECG	Strength/Acceleration (value ($\mu\text{m}/\text{s}^2$))
A	Beginning of atrial systole	The middle of the T-P interval	Maximum to begin diastole (0.145)
B	Beginning of the second stage of ventricular diastole	Peak of the P wave	Zero strength (0)
C	Beginning of ventricular systole	Peak of the R wave	Maximum to begin ventricular systole (-0.196)
D	Beginning of atrial diastole	Beginning of the T wave	Maximum to begin atrial diastole (0.213)
E	End of ventricular systole	End of the T wave	Maximum to begin diastole (0.215)

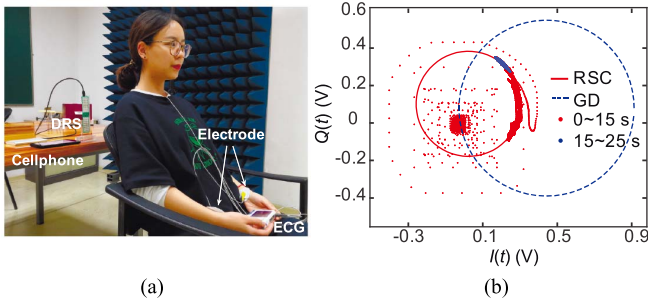


Fig. 10. Experimental setup and environment. (a) Experimental setup. (b) Normalized I/Q signals detected by DRS when the subject sat still on a chair.

atrial and ventricular volume changes. The correspondence between the DCG, ECG, and cardiac activities is summarized in Table II.

In practice, the P-R and R-R intervals, which describe the intervals between the P wave and the R wave and the intervals between the adjacent R waves, respectively, are basics for characterizing heart rate variability (HRV) [2]. To compare the accuracy of the detected DCG with respect to the ECG, the best method is to compare the P-R and R-R intervals retrieved from the ECG and DCG, as shown in Fig. 12. It can be seen that the difference between the averages of the R-R and P-R intervals calculated based on the ECG and DCG are very small. The root mean square error (RMSE) and the normalized RMSE (NRMSE) with respect to the ECG are 14.67 ms/1.9% and 8.58 ms/9.0%, respectively. The relatively larger P-R interval error may be caused by the interfering random body movement in 10–13 cycles of the DCG. The corresponding

TABLE III
INFORMATION OF SUBJECTS

Subject	Gender	Age (year)	Height (cm)	Weight (kg)
1	Female	24	166	56
2	Male	23	181	70
3	Male	27	177	65
4	Female	22	168	57.5

RMSE and NRMSE for 1–9 cycles are 6.44 ms and 6.74%, respectively.

Finally, to verify the reproducibility of the remote DCG detection, the same measurements were performed to four other subjects. The retrieved DCGs and the information of such subjects are shown in Fig. 13 and Table III, respectively. It is seen that the DCGs can be stably detected for different subjects. Based on the corresponding dents on the $v(t)$ curves, using the same method, the B points on the DCGs were also located by aligning the corresponding dents. Note that in all the CPs, identifying the B point is most important and difficult. It is seen that except for the B point in the seventh cycle in panel I, all the B points on the four DCGs can be convincingly identified.

It is also interesting to see that the DCGs detected from different subjects are also different. This result supports the research on cardiac signal-based authentication [38], [43].

D. Discussion

The abovementioned measurement verified our hypothesis on the inner connection between the bioelectric and mechanic cardiac activities of human hearts. It demonstrated

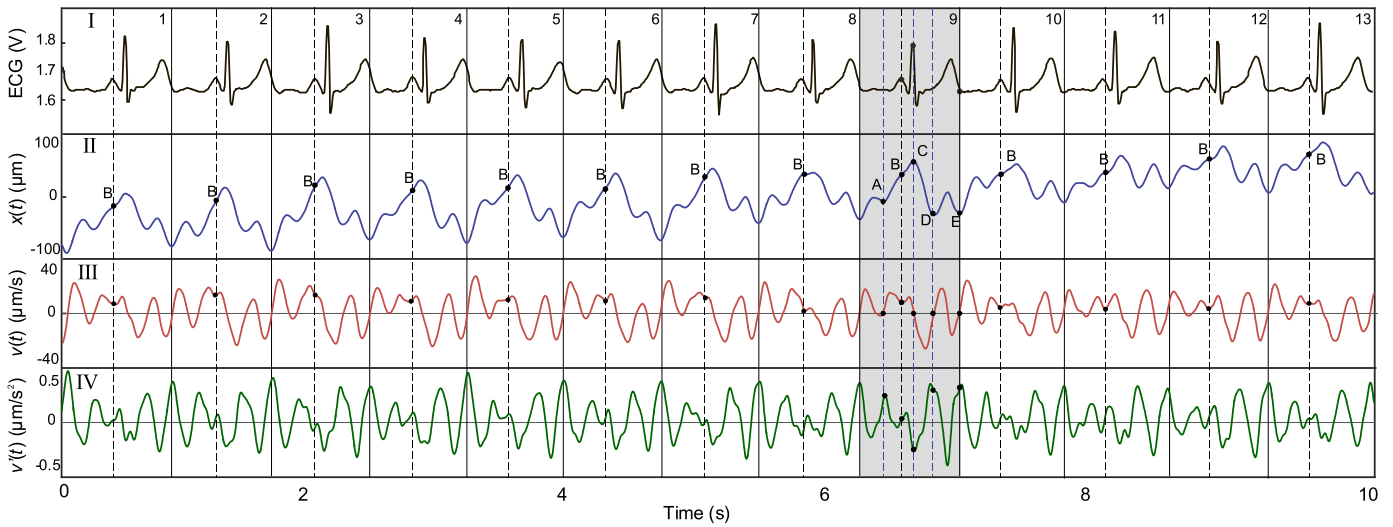


Fig. 11. Comparison between the detected ECG and the DCG.

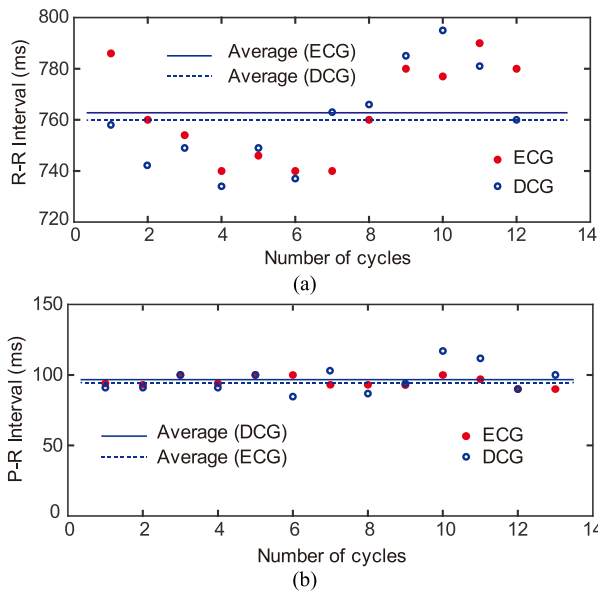


Fig. 12. Comparison between the heart rhythms retrieved from the ECG and DCG. (a) R-R interval. (b) P-R interval.

the possibility to describe the rhythmic cardiac motion using DCGs. Compared with the ECG shown in panel I of Fig. 11, all the timing information of the P-wave, QRS-waves, and T-wave can be extracted from the DCG. In the meantime, the DCG also reflects the displacement (volume change), velocity (change rate), and the acceleration (strength) of the 3-D cardiac motion “projected” on the skin. Such new cardiac information can be potentially used in diagnosis in the future.

In the abovementioned remote measurement, both the K-band DRS and the statistical RSC algorithm previously used in computer visions played important roles. Assisted by the 24-GHz working frequency and 36-dB combined gain provided by the transmitting and receiving antennas and the accurate compensation of the dc offsets, a DRS with a very high linearity and a 4- μm sensitivity can be obtained to detect

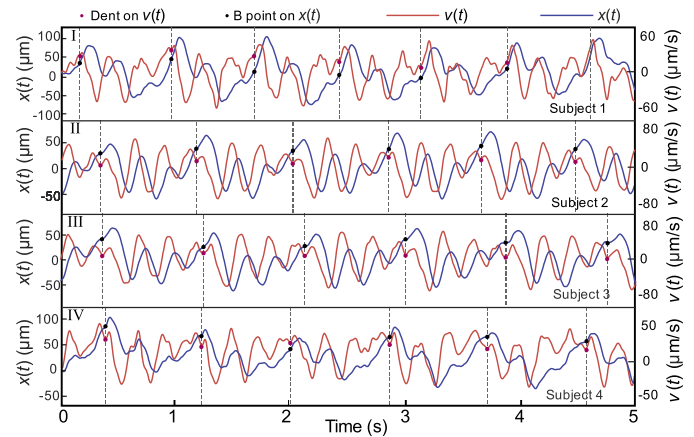


Fig. 13. Experiments for the verification of the reproducibility.

the 100- μm level skin motions. The miniaturized DRS can be potentially integrated into mobile devices, such as pads and smartphones, acting as ideal portable medical instruments.

Major interferences to Doppler cardiac motion detections are unwanted motions, especially burst motions such as a hand movement during a measurement. In this article, we introduced the statistical RSC algorithm previously used in computer visions to eliminate such interfering motions. According to [32], even when the occupation of burst interferences reaches 80% of the sampling period, their impacts can be statistically eliminated, no matter the amplitudes of such interferences. As a statistical approach, the RSC algorithm is essentially different from the existing methods aiming to compensate for dc offsets due to unbalanced I/Q signals and stationary scatterings. Both simulation and experimental results showed excellent performance. This characteristic makes it suitable for medical applications where unwanted motions always happen.

Linearity and sensitivity are the most important specifications describing the ability for a Doppler sensor to

measure ultraweak motion signals. To measure such specifications, a purely sinusoidal μm -scale motion is needed. In physics, the small-amplitude pendulum motion can be considered as an ideal sinusoidal motion. Taking advantage of this characteristic, we proposed a novel, easy-to-manipulate pendulum-based approach to quantitatively determine the linearity and μm -level sensitivity, to evaluate its ability to detect ultraweak motions. This simple and effective approach can be widely used in the Doppler radar sensing community.

In this article, the DCG was remotely detected from the back of the subject with a distance up to 1 m. Experiments showed that for the same DRS, the DCG detected from the front side would not obtain satisfactory results. In most cases, only the A and C points can be detected. According to physiology, human hearts are typically tilted forward and to the left. In this case, the atrial motions that can be detected would be very weak. This result also showed the difference from the noncontact microwave apexcardiogram (ACG) [42], which was detected from the front side of the chest skin with a 3-cm distance.

Unlike ECGs detected with multiple contact electrodes, only a single DRS can be used to detect the DCG. In this *ab initio* study, the stabilities of the DCG waveforms and the R-R and P-R intervals were not as good as those detected by the ECG instrument. Although the amplitude of the detected DCG is 100- μm level, the 4- μm sensitivity is still inadequate to describe the slope change around the B point in the P-wave region. It is seen that while some B points are directly observable in some DCG cycles, some of them need to be located by aligning the dents. For the 4- μm sensitivity, if the change of the slope around a B point was smaller than 4 μm , it could not be detected, resulting in a smoothed slope on which the B point is not easily identified. This could be the source of the relatively large errors of the P-R and R-R intervals of the detected DCG.

To improve such measurement stability, the sensitivity of the DRS can be further improved. In the future, DRSs working at frequencies much higher than 24 GHz could be used to improve the 4- μm sensitivity to submicrometer level. Signal processing algorithms used in detecting weak bioelectrical signals can also be used to improve the SNR of the detected signal carrying Doppler information. We believe that the proposed DCG will reach a much higher accuracy in the future.

Finally, while we have experimentally demonstrated the detection of the B points for different subjects, it is possible that for certain subjects, the B points could be simply invisible. However, it also means that such subjects can be differentiated from "normal" subjects whose B points can be detected. It implies the potential to use DCGs in heart-type classification and heart disease diagnoses. At this stage, convincing DCG detections in the present of respirations is also difficult. It deserves future research efforts.

IV. CONCLUSION

In conclusion, we pointed out the feasibility of the remote measurement of a new type human cardiogram, the DCG, by detecting the combined atrial and ventricular contractions and relaxations conducted to the skin on the back chest.

A K-band, board-integrated DRS was then designed and implemented to experimentally verify this possibility. The obtained DCG can be used to detect both the heart rhythm and cardiac motion information, having promising potentials in extended applications such as hospitalization, personal daily healthcare, battlefield rescue, and cardiosignal-based authentication.

REFERENCES

- [1] D. Stuckler, "Population causes and consequences of leading chronic diseases: A comparative analysis of prevailing explanations," *Milbank Quart.*, vol. 86, no. 2, pp. 273–326, Jun. 2008.
- [2] W. Massagram, O. Boric-Lubecke, L. Macchiarulo, and M. Chen, "Heart rate variability monitoring and assessment system on chip," in *Proc. IEEE 27th Annu. Conf. Eng. Med. Biol. Soc.*, Jan. 2006, pp. 7369–7372.
- [3] M. Alghatrif and J. Lindsay, "A brief review: History to understand fundamentals of electrocardiography," *J. Community Hospital Internal Med. Perspect.*, vol. 2, no. 1, p. 14383, Apr. 2012.
- [4] N. S. Anavekar, D. Gerson, H. Skali, R. Y. Kwong, E. K. Yucel, and S. D. Solomon, "Two-dimensional assessment of right ventricular function: An echocardiographic-MRI correlative study," *Echocardiography*, vol. 24, no. 5, pp. 452–456, 2007.
- [5] R. P. Paiva *et al.*, "Beat-to-beat systolic time-interval measurement from heart sounds and ECG," *Physiol. Meas.*, vol. 33, no. 2, pp. 177–194, 2012.
- [6] G. Cybulski, E. Michalak, E. Kozluk, A. Piatkowska, and W. Niewiadomski, "Stroke volume and systolic time intervals: Beat-to-beat comparison between echocardiography and ambulatory impedance cardiography in supine and tilted positions," *Med. Biol. Eng. Comput.*, vol. 42, no. 5, pp. 707–711, 2004.
- [7] O. T. Inan *et al.*, "Ballistocardiography and seismocardiography: A review of recent advances," *IEEE J. Biomed. Health Inform.*, vol. 19, no. 4, pp. 1414–1427, Jul. 2015.
- [8] X. Guo, M. Liu, Z. Ma, Y. Yang, and T. Zhang, "Assessing right ventricular function in patients with pulmonary hypertension based on noninvasive measurements: Correlation between cardiac MRI, ultrasonic cardiogram, multidetector CT and right heart catheterization," *J. Cardiovascular Magn. Reson.*, vol. 17, no. 1, p. P185, Feb. 2015.
- [9] S. E. Luijnenburg *et al.*, "Abnormal right atrial and right ventricular diastolic function relate to impaired clinical condition in patients operated for tetralogy of Fallot," *Int. J. Cardiol.*, vol. 167, no. 3, pp. 833–839, 2013.
- [10] A. Anghel, G. Vasile, R. Cacoveanu, C. Ioana, and S. Ciochina, "Short-range wideband FMCW radar for millimetric displacement measurements," *IEEE Trans. Geosci. Remote Sens.*, vol. 52, no. 9, pp. 5633–5642, Sep. 2014.
- [11] S. Jarak *et al.*, "Detection and localization of multiple short range targets using FMCW radar signal," in *Proc. Global Symp. Millim. Waves (GSMW), ESA Workshop Millim.-Wave Technol. Appl.*, Jun. 2016, pp. 1–4.
- [12] J. Wang, X. Wang, Z. Zhu, J. Huangfu, C. Li, and L. Ran, "1-D microwave imaging of human cardiac motion: An *ab-initio* investigation," *IEEE Trans. Microw. Theory Techn.*, vol. 61, no. 5, pp. 2101–2107, May 2013.
- [13] Q. Lv *et al.*, "High dynamic-range motion imaging based on linearized Doppler radar sensor," *IEEE Trans. Microw. Theory Techn.*, vol. 62, no. 9, pp. 1837–1846, Sep. 2014.
- [14] F.-K. Wang *et al.*, "A novel vital-sign sensor based on a self-injection-locked oscillator," *IEEE Trans. Microw. Theory Techn.*, vol. 58, no. 12, pp. 4112–4120, Dec. 2010.
- [15] N. Pohl *et al.*, "Radar measurements with micrometer accuracy and nanometer stability using an ultra-wideband 80 GHz radar system," in *Proc. IEEE Top. Conf. Wireless Sensors Sensor Netw. (WiSNet)*, Jan. 2013, pp. 31–33.
- [16] A. Zhu, T. Fan, Z. Gu, Q. Lv, C. Li, and L. Ran, "Indoor localization based on a single-tone SIMO-structured Doppler radar system," *IEEE J. Emerg. Sel. Topics Circuits Syst.*, vol. 8, no. 2, pp. 271–279, Jun. 2018.
- [17] Z. Gu *et al.*, "Remote blind motion separation using a single-tone SIMO Doppler radar sensor," *IEEE Trans. Geosci. Remote Sens.*, vol. 57, no. 1, pp. 462–472, Jan. 2019.
- [18] L. Ren, H. Wang, K. Naishadham, Q. Liu, and A. E. Fathy, "Non-invasive detection of cardiac and respiratory rates from stepped frequency continuous wave radar measurements using the state space method," in *IEEE MTT-S Int. Microw. Symp. Dig.*, May 2015, pp. 1–4.

- [19] N. Hafner, J. C. Drazen, and V. M. Lubecke, "Fish heart rate monitoring by body-contact Doppler radar," *IEEE Sensors J.*, vol. 13, no. 1, pp. 408–414, Jan. 2012.
- [20] B. Spencer, Jr., S. Cho, and S.-H. Sim, "Wireless monitoring of civil infrastructure comes of age," *Structure*, vol. 13, pp. 12–16, Oct. 2011.
- [21] M. Pieraccini, M. Fratini, F. Parrini, and C. Atzeni, "Dynamic monitoring of bridges using a high-speed coherent radar," *IEEE Trans. Geosci. Remote Sens.*, vol. 44, no. 11, pp. 3284–3288, Nov. 2006.
- [22] Q. Wan, Y. Li, C. Li, and R. Pal, "Gesture recognition for smart home applications using portable radar sensors," in *Proc. 36th Annu. Int. Conf. IEEE Eng. Med. Biol. Soc.*, Aug. 2014, pp. 6414–6417.
- [23] A. Naqvi, S.-T. Yang, and H. Ling, "Investigation of Doppler features from wind turbine scattering," *IEEE Antennas Wireless Propag. Lett.*, vol. 9, pp. 485–488, 2010.
- [24] V. C. Chen, F. Li, S.-S. Ho, and H. Wechsler, "Micro-Doppler effect in radar: Phenomenon, model, and simulation study," *IEEE Trans. Aerosp. Electron. Syst.*, vol. 42, no. 1, pp. 2–21, Jan. 2006.
- [25] N. Whiteloni, S.-T. Yang, and H. Ling, "Application of near-field to far-field transformation to Doppler features from wind turbine scattering," *IEEE Trans. Antennas Propag.*, vol. 60, no. 3, pp. 1660–1665, Mar. 2012.
- [26] A. D. Droitcour, O. Boric-Lubecke, V. M. Lubecke, J. Lin, and G. T. A. Kovacs, "Range correlation and I/Q performance benefits in single-chip silicon Doppler radars for noncontact cardiopulmonary monitoring," *IEEE Trans. Microw. Theory Techn.*, vol. 52, no. 3, pp. 838–848, Mar. 2004.
- [27] J. Wang, X. Wang, L. Chen, J. Huangfu, C. Li, and L. Ran, "Noncontact distance and amplitude-independent vibration measurement based on an extended DACM algorithm," *IEEE Trans. Instrum. Meas.*, vol. 63, no. 1, pp. 145–153, Jan. 2014.
- [28] T. Fan *et al.*, "Wireless hand gesture recognition based on continuous-wave Doppler radar sensors," *IEEE Trans. Microw. Theory Techn.*, vol. 64, no. 11, pp. 4012–4020, Nov. 2016.
- [29] J. T. Ottesen, M. S. Olufsen, and J. Larsen, *Applied Mathematical Models in Human Physiology*. Philadelphia, PA, USA: Society for Industrial and Applied Mathematics, 2004, pp. 15–20.
- [30] A. M. Katz, *Physiology of the Heart*, 2nd ed. New York, NY, USA: Raven Press, 1992.
- [31] Q. Lv *et al.*, "Doppler vital signs detection in the presence of large-scale random body movements," *IEEE Trans. Microw. Theory Techn.*, vol. 66, no. 9, pp. 4261–4270, Sep. 2018.
- [32] M. A. Fischler and R. Bolles, "Random sample consensus: A paradigm for model fitting with applications to image analysis and automated cartography," *Commun. ACM*, vol. 24, no. 6, pp. 381–395, 1981.
- [33] Z. Peng, L. Ran, and C. Li, "A 24-GHz low-cost continuous beam steering phased array for indoor smart radar," in *Proc. IEEE 58th Int. Midwest Symp. Circuits Syst. (MWSCAS)*, Fort Collins, CO, USA, Aug. 2015, pp. 1–4.
- [34] K. G. Derpanis, "Overview of the RANSAC algorithm," Dept. Comput. Sci., York Univ., Toronto, ON, Canada, Tech. Rep. 4, May 2010.
- [35] R. Nelson and M. G. Olsson, "The pendulum—Rich physics from a simple system," *Amer. J. Phys.*, vol. 54, no. 2, pp. 112–121, Feb. 1987.
- [36] H. David, R. Resnick, and J. Walker, *Fundamentals of Physics*, 5th ed. New York, NY, USA: Wiley, 1997, p. 381.
- [37] A. Ragman, V. M. Lubecke, O. Boric-Lubecke, J. H. Prins, and T. Sakamoto, "Doppler radar techniques for accurate respiration characterization and subject identification," *IEEE J. Emerg. Sel. Topics Circuits Syst.*, vol. 8, no. 2, pp. 350–359, Jun. 2018.
- [38] B. Park, O. Boric-Lubecke, and V. M. Lubecke, "Arctangent demodulation with DC offset compensation in quadrature Doppler radar receiver systems," *IEEE Trans. Microw. Theory Techn.*, vol. 55, no. 5, pp. 1073–1079, Jun. 2007.
- [39] S. Kim and C. Nguyen, "On the development of a multifunction millimeter-wave sensor for displacement sensing and low-velocity measurement," *IEEE Trans. Microw. Theory Techn.*, vol. 52, no. 11, pp. 2503–2512, Nov. 2004.
- [40] C. Gu, C. Li, J. Lin, J. Long, J. Huangfu, and L. Ran, "Instrument-based noncontact Doppler radar vital sign detection system using heterodyne digital quadrature demodulation architecture," *IEEE Trans. Instrum. Meas.*, vol. 59, no. 6, pp. 1580–1588, Jun. 2010.
- [41] C. Li, Y. Xiao, and J. Lin, "Experiment and spectral analysis of a low-power Ka-band heartbeat detector measuring from four sides of a human body," *IEEE Trans. Microw. Theory Techn.*, vol. 54, no. 12, pp. 4464–4471, Dec. 2006.
- [42] J. C. Lin, J. Kiernicki, M. Kiernicki, and P. B. Wollschlaeger, "Microwave apexcardiography," *IEEE Trans. Microw. Theory Techn.*, vol. MTT-27, no. 6, pp. 618–620, Jun. 1979.
- [43] F. Lin, C. Song, Y. Zhuang, W. Xu, C. Li, and K. Ren, "Cardiac scan: A non-contact and continuous heart-based user authentication system," in *Proc. 23rd Annu. Int. Conf. Mobile Comput. Netw.*, Oct. 2017, pp. 315–328.